ACADEMIC PRESS

Available online at www.sciencedirect.com

SCIENCE DIRECT®

Journal of Structural Biology 141 (2003) 9–21

Journal of Structural Biology

www.elsevier.com/locate/yjsbi

X-ray microCT study of pyramids of the sea urchin *Lytechinus variegatus*

S.R. Stock,[a,*] S. Nagaraja,[b] J. Barss,[c] T. Dahl,[c] and A. Veis[c]

[a] *Institute for Bioengineering and Nanoscience in Advanced Medicine, Northwestern University, 303 E. Chicago Avenue, Tarry 16-717, Chicago, IL 60611-3008, USA*

[b] *School of Mechanical Engineering, Georgia Institute of Technology, Atlanta, GA 30332, USA*

[c] *Department of Cell and Molecular Biology, Northwestern University, Chicago, IL 60611, USA*

Received 19 June 2002, and in revised form 23 September 2002

Abstract

This paper reports results of a novel approach, X-ray microCT, for quantifying stereom structures applied to ossicles of the sea urchin *Lytechinus variegatus*. MicroCT, a high resolution variant of medical CT (computed tomography), allows noninvasive mapping of microstructure in 3-D with spatial resolution approaching that of optical microscopy. An intact pyramid (two demi-pyramids, tooth epiphyses, and one tooth) was reconstructed with 17 μm isotropic voxels (volume elements); two individual demipyramids and a pair of epiphyses were studied with 9–13 μm isotropic voxels. The cross-sectional maps of a linear attenuation coefficient produced by the reconstruction algorithm showed that the structure of the ossicles was quite heterogeneous on the scale of tens to hundreds of micrometers. Variations in magnesium content and in minor elemental constitutents could not account for the observed heterogeneities. Spatial resolution was insufficient to resolve the individual elements of the stereom, but the observed values of the linear attenuation coefficient (for the 26 keV effective X-ray energy, a maximum of 7.4 cm^{-1} and a minimum of ~2 cm^{-1} away from obvious voids) could be interpreted in terms of fractions of voxels occupied by mineral (high magnesium calcite). The average volume fraction of mineral determined for a transverse slice of the demipyramid near where it joins an epiphysis was 0.46; for a slice 3.3 mm adoral it was 0.70. Local volume fractions of mineral approached 1, and, away from resolvable voids, considerable portions of the demipyramids had volume fractions of calcite at or below ~0.33. MicroCT imaging of a demipyramid before and after infiltration with a high absorptivity fluid (sodium polytungstate) confirmed the determination of the volume fractions of minerals.

© 2002 Elsevier Science (USA). All rights reserved.

Keywords: *Lytechinus variegatus*; Microtomography (microCT); Sea urchin; Pyramid; X-ray; Ossicle; Calcite

1. Introduction

Sea urchin teeth are exquisitely designed, self-renewing composites (Märkel, 1969, 1970a,b; Märkel and Titschack, 1969; Märkel et al., 1976; Wang et al., 1997), but much of their functionality arises from the oral apparatus (Aristotle's lantern) holding them (Fig. 1). Aristotle's lantern, a distinctive feature of Echinoida believed important in their evolutionary success (Jackson, 1912; Smith, 1984), consists of five sets of ossicles and associated muscles (e.g., Jackson, 1912; Candia Carnevali et al., 1991, 1993), and, within each set, the largest of the bone-like, calcite (calcium carbonate) structures is the pyramid. Each pyramid incorporates a pair of complementary demipyramids and a pair of complementary epiphyses and, in regular echinoids, has a well-defined plane of symmetry along the junction of the matching pair of demipyramids. Enclosed in the pyramid, the tooth follows the plane of symmetry and attaches to the dental slide which follows the pyramidal suture. Unlike the fiber and lamella reinforcement of the teeth, the pyramid and most of the other mineralized tissues of the sea urchin (test, spines) achieve high specific strength (strength-to-weight ratio) and toughness through partition of the structure into varying volume fractions of stereom (fenestrated or trabecular mineral) and stroma (fluid, investing soft tissue including extracellular fibrils and

* Corresponding author. Fax: 1-312-503-2544.
E-mail address: s-stock@northwestern.edu (S.R. Stock).

1047-8477/02/$ - see front matter © 2002 Elsevier Science (USA). All rights reserved.
PII: S1047-8477(02)00554-3

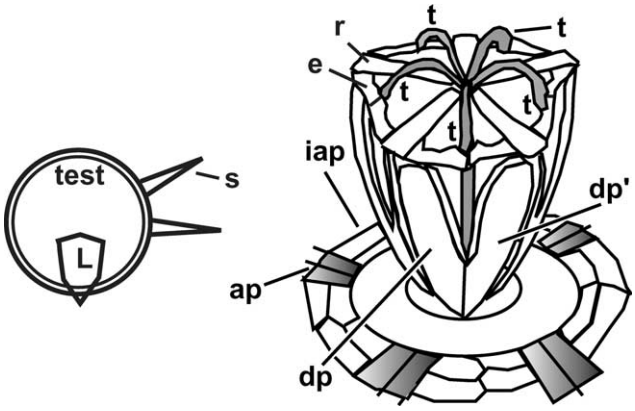

Fig. 1. Geometry of Aristotle's lantern of a regular sea urchin. (Left) Side view of the sea urchin test showing spines "s" and lantern "L". (Right) Strucutre of the lantern, opening in the test through which the lantern protrudes during feeding and interambulacral "ipa" and ambulacral "ap" plates surrounding the opening. Due to their small size, the individual ambulacral plates are not shown but are indicated by shading. A pair of complementary demipyramids "dp" and "dp" are on the face of the lantern closest to the viewer, and all five teeth "t" of the lantern are labeled. An epiphysis "e" and a rotula "r" are also labeled. The adoral ends of lantern and teeth point down in this schematic.

connective tissue). Camarodont echinoids, such as *Lytechinus variegatus*, the subject of the present report, realize additional weight saving in the oral apparatus; cavities extend deeply into the demipyramids; and large openings in the external pyramid wall, foramina magna, replace much of the ossicle volume seen in cidarids.

In the sea urchin, various skeletal components (other than teeth) and, indeed, different portions of each ossicle develop multiple types of three-dimensional meshwork in response to specific functional requirements. Smith (1980) comprehensively categorized the different stereom structures and mapped their occurrence in echinoid tests and spines; Smith (1980, 1990) also quantified pore diameter vs trabecular thickness for echinoids and for other echinoderms. Candia Carnevali and co-workers investigated stereom types in camarodont (1991) and cidarid (1993) lanterns. To date, SEM (scanning electron microscopy) was used after soft tissue removal to study the surface stereom and, to a lesser extent, the internal fenestrated structure, and it appears that the focus of earlier studies was on aspects other than mapping variations in mineral density in the fine structure of lantern ossicles.

This paper reports results of a novel approach for quantifying stereom structure, microCT (micro-computed tomography, a high resolution variant of medical CT, also termed microtomography), to an intact section of Aristotle's lantern (one pyramid comprised of a tooth attached to a pair of demipyramids and associated epiphyses) of an adult of short-spined sea urchin *L. variegatus*. MicroCT images the 3-D microstructure with spatial resolution approaching that of optical microscopy. A series of views through the sample (i.e., radiographs recorded along different directions) are recombined mathematically into a cross-sectional map of the specimen's X-ray absorptivity; techniques, instrumentation, and past applications are summarized elsewhere (Stock, 1999). X-ray microCT units are commercially available, and two such systems were used here to quantify the distribution of mineral in pyramid and epiphyseal stereom, noninvasively and as a function of 3-D position within pyramids and ephiphyses. Earlier, Stock et al. (2002a, 2002b) applied X-ray methods (absorption microCT, diffraction mapping with a small diameter beam of synchrotron radiation, and phase contrast microradiography with synchrotron radiation) to study the microstructure of *L. variegatus* teeth, and the work reported below is, to the best of the authors' knowledge, the first employing microCT to study ossicles, other than teeth, of Aristotle's lantern. The structural data developed provide a unique insight into the architectural and compositional complexity of the lantern stereom, every bit as exquisitely designed for its mechanical function as the teeth it holds.

2. Materials and methods

Two types of specimens were examined (Table 1). The first specimen was an intact pyramid (tooth, pair of demipyramids, and pair of epiphyses) dissected from an adult sea urchin (*L. variegatus*) and fixed in isopropanol in a sealed plastic vial. The second type of specimens were from a sea urchin which died in an aquarium of natural causes; the ossicles of the lantern fell from the test and lay on the tank bottom for at least a week before they were collected and dried in air. The two demipyramids were imaged individually in air, as were a pair of epiphyses positioned as they would be in an intact lantern. In addition to identifying the samples, Table 1 also lists the imaging conditions.

The intact pyramid was scanned with a Scanco MicroCT-40 system operated at 50 kV and 80 μA; the X-ray focal spot was about 10 μm in diameter. The 16.4 mm horizontal field of view was sampled with 1024 increments and 500 angular views with 0.3 s integration time per view. Slices were recorded every 16–17 μm and were reconstructed with 16×16 μm voxels (volume elements) in plane.

The individual demipyramids and the pair of epiphyses were scanned with a Scanco MicroCT-20 system operated at 50 kV; the effective X-ray energy was nominally 30 keV. Integration time of 0.35 s, 500 projections per slice, 1024 samples per projection, and 25 μm slice thickness were used. For demipyramid 3, reconstruction was with 9 μm in-plane voxel size and 100 μm spacing between slices; for demipyramid 5 the values were 11 and 100 μm, respectively, and for the pair of epiphyses 13 and 25 μm, respectively.

Table 1
Summary of samples and imaging conditions

Specimen	Environment	Apparatus	t	In-plane voxel size	Slice spacing
Intact pyramid	Isopropanol	40	0.3	16	16
Demipyramid 3	Air	20	0.35	9	100
Demipyramid 5	Air	20	0.35	11	100
	Polytungstate	20	0.35	11	100
Pair of epiphyses	Air	20	0.35	13	25

All measurements were conducted at 50 kV, with 1024 samples of the horizontal field of view and 500 projections per slice. Data collected with a MicroCT-40 (20) system are indicated by 40 (20), the integration time t is in seconds, and the voxel size and slice spacing are in micrometer.

Because many of the pores in the stereom were too small to be resolved as discrete entities with a laboratory (i.e., nonsynchrotron) X-ray microCT system, the observed values of the linear attenuation coefficient must be interpreted in terms of the fraction of voxel occupied by high magnesium calcite and the fraction occupied by soft tissue, in the case of the intact lantern, or by empty space, in the case of the ossicles from which the soft tissue had been removed by natural processes. This interpretation appears under Section 4 and makes use of additional measurements outlined below.

Use of high absorption fluids to enhance visibility of low contrast features is a standard technique (e.g., arteries in medical radiology and cracks in composites in industrial radiography), and this approach can quantify the fraction of a voxel occupied by stereom (calcite) if the linear attenuation coefficients within the same volume of an ossicle are mapped before and after infiltration with a liquid with a known X-ray absorptivity (say, intermediate between fully dense calcite and stroma). Therefore, subsequent to collection of the first data set, between 5 and 10 mm of the adoral end of demipyramid 5 was immersed in a 6% solution of polytungstate (Geoliquids, Prospect Heights, IL; 5.0 g of $3Na_2WO_4 \cdot 9WO_3 \cdot H_2O$, density 2.89 g/cm^3, in 33.6 ml distilled H_2O; solution density 1.083 g/cm^3), and capillary action pulled the solution into the ossicle's pores. After infiltration, demipyramid 5 was imaged again using the same parameters as in the first data set. Note that some solution remained outside of the demipyramid and provided a direct measure of the linear attenuation coefficient of the solution.

Measurements on a millimeter-sized, inorganic calcite crystal revealed the effective energy to be about 26 keV (Stock et al., 2002b). This provided an independent reference, free of organic material, for $Ca_{1-x}Mg_xCO_3$ with $x = 0$.

3. Results

The 3-D geometry of the demipyramids, the epiphyses, and the intact pyramid are best introduced using 3-D renderings derived from the microCT data. The 3-D renderings of the intact pyramid shown in Fig. 2 were produced with Scanco's proprietary software, and the three images illustrate its structure preparatory to detailed discussion of individual slices. The tooth spans 22.4 mm from its oral end (bottom of Fig. 2, with the adoral direction indicated by the arrow labeled "ad") to its curved aboral end (top of Fig. 2, aboral direction shown by the arrow designated "ab"). The left-hand image shows one of the five pyramids of Aristotle's lantern; its center is to the right of the rendered volume; here the adaxial side of the tooth appears ("t_{ada}" in Fig. 2). The middle and right-hand images of Fig. 2 show different views of structures revealed only when obscuring solid is numerically removed.

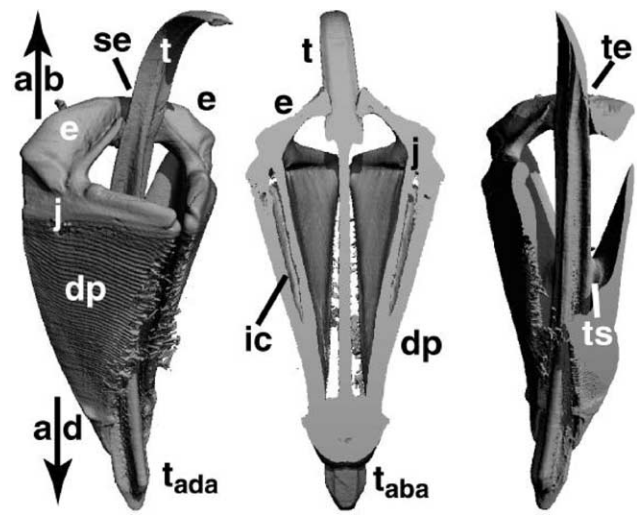

Fig. 2. Three-dimensional renderings based from the microCT slices (16 μm in-plane voxels) of the intact pyramid. In the left-hand image, the tooth "t" spans 22.4 mm. The middle and right-hand images are viewed after numerical sectioning to expose internal structure.

A regular array of parallel ridges appear on the outside of the demipyramid in the left-hand rendering of Fig. 2; the interpyramidal muscles attach to the ridge area. The wide foramen magnum, the large opening in the tangential wall of the pyramid, i.e., the external wall of the lantern, is visible behind the tooth in the left-hand and right-hand renderings. Other features important in the data presented below and labeled in Fig. 2 include the suture between epiphyses ("se" in the left-hand rendering), the interface between epiphysis "e" and demipyramid "dp" ("j" in the left-hand rendering), the

intrapyramidal cavities ("ic" in the middle image), the contact between epiphyses and tooth "t" (between "t" and "e" in the middle and "te" in the right-hand images), and the dental slide-tooth junction ("ts" in the right-hand rendering).

Fig. 3 shows 10 slices through the epiphyses of the intact pyramid; every 16th slice is included with the number of the slice appearing in the lower right corner of each image. In all of the figures showing slices, the lighter the pixel, the higher the linear attenuation coefficient in that voxel. An image from an epiphysis from a decomposed sea urchin (labeled "ref" in Fig. 3) appears above that of slice 322. The tooth "t" is labeled in slice 418, and the keel of the tooth has just begun to develop in the most aboral slice shown (slice 290). A narrow band of low absorptivity was noted previously by Stock et al. (2002a, 2002b) to run across the flange, and this band can be seen in higher magnification views of slice 290 although not in that used in Fig. 3. The epiphyseal suture "se" in slice 290 appears to consist of two narrow bands of higher attenuation separated by lower attenuation material. This structure does not persist, however, through the epiphyses. Slices 306, 322, and 338 show a coarse structure consisting of an array of parallel, high absorptivity, high-aspect-ratio features "l" on either side of the suture (i.e., white, somewhat irregular stripes), and Fig. 4 enlarges slices 290, 322, and 354 to show the structure more clearly. The zone "l" is bounded by a fairly wide ring of low absorption material, and the outer surface of the ossicle has higher absorptivity. The same type of contrast is seen in the reference slice, albeit less clearly due to data collection at lower spatial resolution. The contact "te" between tooth and epiphyses appears to extend over at least slices 322 through 370. Note that the structure "l" is not associated solely with the suture but is clear up past the tooth-epiphyses confluence and to about the point where the horns "h" of demipyramids attach to the epiphyses.

The three slices shown in Fig. 5 illustrate the structural transition from the foramen magnus (slice 642) to the dental slide (slices 786 and 914) and span just under 4.5 mm of the intact pyramid. Low absorptivity material

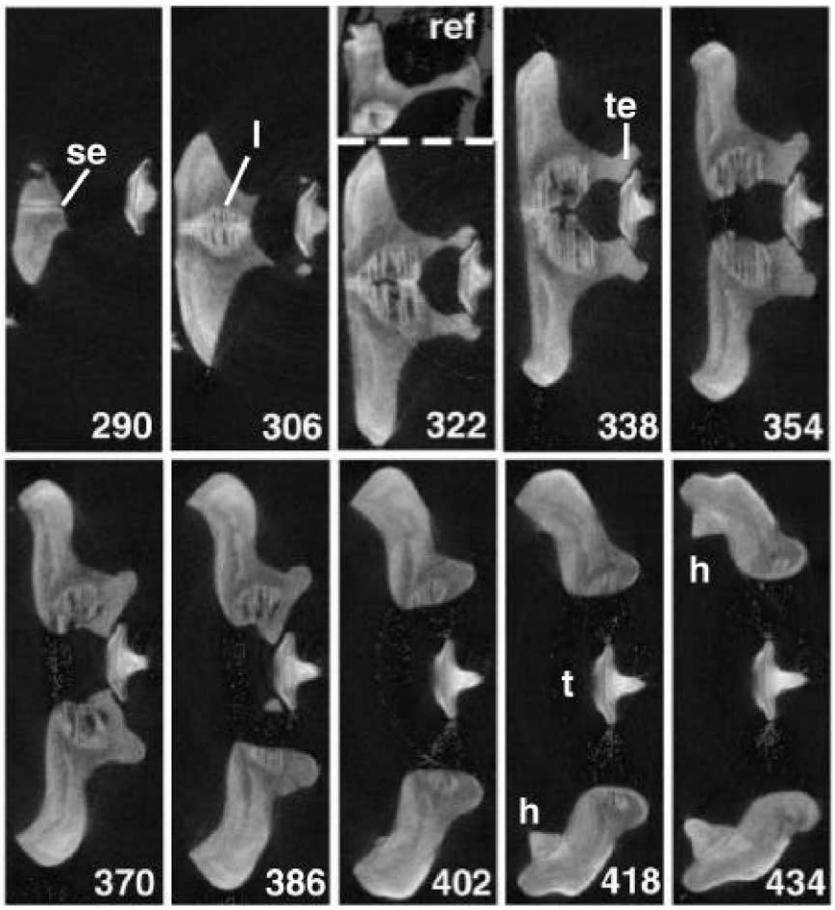

Fig. 3. Slices through the epiphyses in the intact lantern with 16 μm in-plane voxels. The sprinkling of light gray pixels in the empty space between ossicles in this figure (as well as those in Figs. 4–8) are artifacts of conversion to gray-scale images for publication; these are the lowest absorption voxels in the data set and are left to indicate the noise in the reconstructed slices. The reference image "ref" is from one side of a complementary pair of ephiphyses mounted on modeling clay to approximate the epiphyseal position in the intact pyramid; the orientation of the slice, therefore, differs slightly from that in slice 322. The length of the flange of the tooth "t" (vertical in these images) is 1.7 mm.

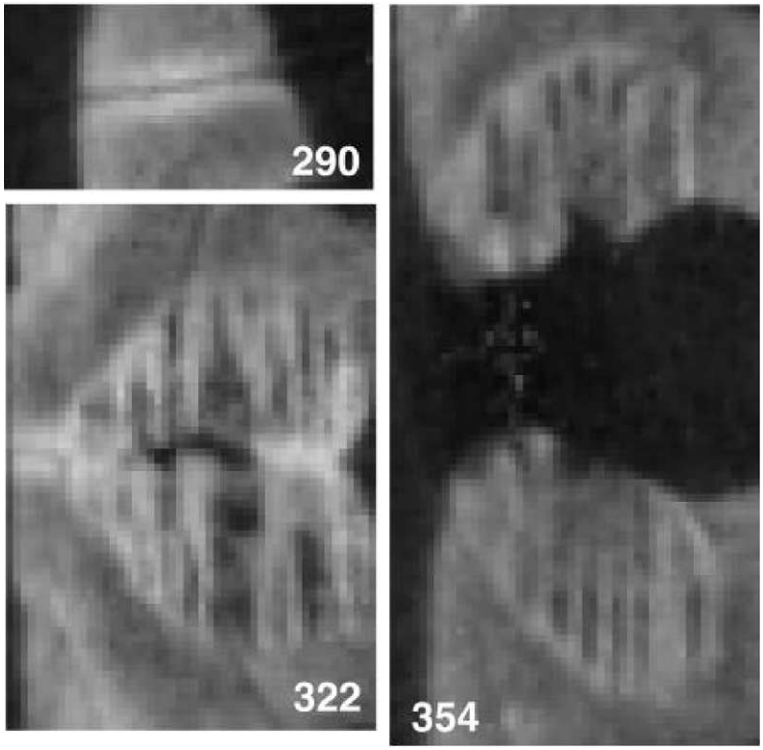

Fig. 4. Enlargement of the area around the epiphyseal suture for three slices of Fig. 3. The magnification is the same for all of these images, and the horizontal field of view in slice 354 is 0.88 mm.

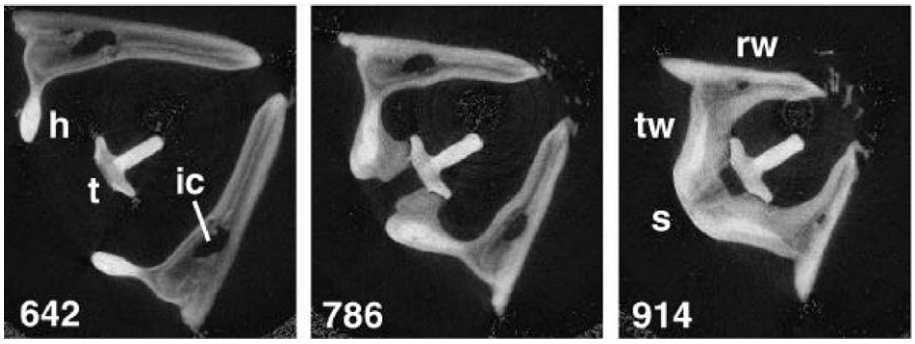

Fig. 5. Three slices through the intact pyramid reconstructed with 16.4 μm in-plane voxel size. The slice number (position) appears in the lower left corner of each image, and the flange of the tooth is 1.7 mm across (here rotated slightly counterclockwise from vertical).

occupies the majority of the interior of the radial walls "rw" of the demipyramids and surrounds the intrapyramidal cavities. Somewhat higher absorptivity voxels occupy the periphery of the ossicles, and long, narrow, high absorptivity bands lie within the low absorptivity material (e.g., in slice 642). The fraction of low absorptivity stereom in the radial walls shrinks adorally, that is, as the pyramid cross section decreases toward its apex. The "horns" of the demipyramids ("h" in slice 642 of Fig. 5 and in slices 418 and 434 of Fig. 3) as well as the bulk of the tangential walls ("tw" in Fig. 5) consist of very high absorptivity stereom. Somewhat lower absorptivity stereom comprises the dental slide (slice 786, Fig. 5) and the triangularly shaped volume surrounding most of the pyramidal suture "s" (slice 914, Fig. 5). Contact between the flange of the tooth and the demipyramids occurs at the pair of pillar bridges in slice 786 (lateral abaxial surface of the tooth); except at these points the lateral portions of the flange lie parallel to the surface of the dental slide. The interradial cavity separates the medial portion of the flange from the demipyramids.

Slice 818 shown in Fig. 6 is about 525 μm adoral from slice 786 and 1.57 mm aboral from slice 914 (see Fig. 5); the smaller image (right) enlarges the area around the dental slide and tooth's flange. The arcs within the image

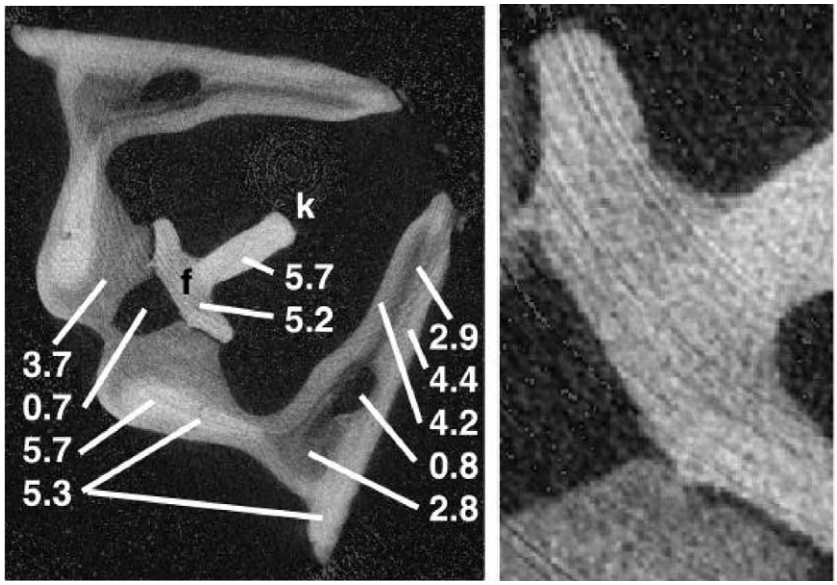

Fig. 6. (Left) Value of the linear attenuation coefficient (cm^{-1}) for different positions within a slice of the intact pyramid. The distance across the flange "f" is 1.7 mm. (Right) Enlargement of the area around the pillar bridges.

of the tooth, stretching from upper left to lower right, are ring artifacts, well known to result from uncorrected nonuniformities in detector response. The numbers in the left-hand image are values of the linear attenuation coefficient (cm^{-1}) for the positions indicated. In the flange of the tooth 'f'', the linear attenuation coefficient is $5.2\,cm^{-1}$ while in the keel it is $5.7\,cm^{-1}$. The high attenuation regions have $5.3\,cm^{-1} < \mu < 5.7\,cm^{-1}$ in the slice shown in Fig. 6. Within the intrapyramidal cavity $\mu = 0.8\,cm^{-1}$ while the void between the tooth's flange and the demipyramids contains voxels with $\mu = 0.7\,cm^{-1}$. Isopropanol typically produces linear attenuation coefficients of 0.7–$0.8\,cm^{-1}$ for the instrument settings used for this sample. The bands of low attenuation stereom in the radial walls of the demipyramids have $\mu = 2.8$–$2.9\,cm^{-1}$ and are surrounded by voxels with linear attenuation coefficients between 4.2 and $4.4\,cm^{-1}$. In the volume bounding the suture between the demipyramids, the linear attenuation coefficient is $3.7\,cm^{-1}$. Conversion of these values to fractions of a voxel occupied by calcite (i.e., stereom) follows under Section 4.

Fig. 7 shows two slices from demipyramid 3 (left image, slice 22, and the right image, slice 54). The radial wall in these slices (extending vertically) is longer than the tangential wall; it is also thicker than the tangential wall. The length of the radial wall decreases from slice 22 to slice 54 (7.1 mm vs 5.6 mm, respectively) which is consistent with the taper of pyramids toward their oral end, and the tangential wall is somewhat longer and narrower in slice 54 compared to slice 22 (lengths of 3.6 mm vs 3.2 mm, respectively). The intrapyramidal cavity covers a large fraction of the area of the radial wall near where it and tangential wall meet. The maximum width of the cavity perpendicular to the radial wall is 900 μm in slice 22 and 600 μm in slice 54; the wall thickness between the cavity and the inner surface of the demipyramid is as low as 50–100 μm. The length of the cavity along the radial direction of the demipyramid is about 2.2 mm in slice 22 and 1.9 mm in slice 54.

Fig. 7 also illustrates the changes in linear attenuation coefficient from fine structure within the demipyramid, particularly within the radial wall. The maximum value was $7.4\,cm^{-1}$ and the minimum, away from resolvable pores, was $\sim 2\,cm^{-1}$. In slice 22 two small cavities are seen adjacent to the large intrapyramidal cavity, and nodules of high absorptivity ($\sim 5.9\,cm^{-1}$ vs $\sim 2\,cm^{-1}$ of the surroundings) are present along the outer surface of the radial wall (outside of the "L"). The inset image on slice 22 enlarges an area near the outside corner of the tangential wall. The three protuberances are the ridges "dp" in Fig. 2 (left), i.e., a portion of the intrapyramidal muscle attachment structure. A narrow band of high absorptivity runs near the center of the radial wall, parallel to the sides of the walls, and the magnitude of μ is similar to that in the nodules. In slice 22, the internal high absorptivity band ($\mu > 5\,cm^{-1}$) is much closer to the inner than the outer surface of the wall; in slice 54 the band appears in the center of the radial wall. In both cases the width of the high absorptivity band is on the order of 100 μm, the surrounding low absorptivity areas are about as wide and the main difference between structures is the high absorptivity shell (inner and outer sides of the radial wall) which is much more uniform and thicker in slice 54 than in slice 22. Within slice 22 of the demipyramid, the highest absorption coefficients occur at the ends of the radial and tangential walls and at the external corner where the radial and tangential walls meet. The absorptivity in slice 54 follows a similar

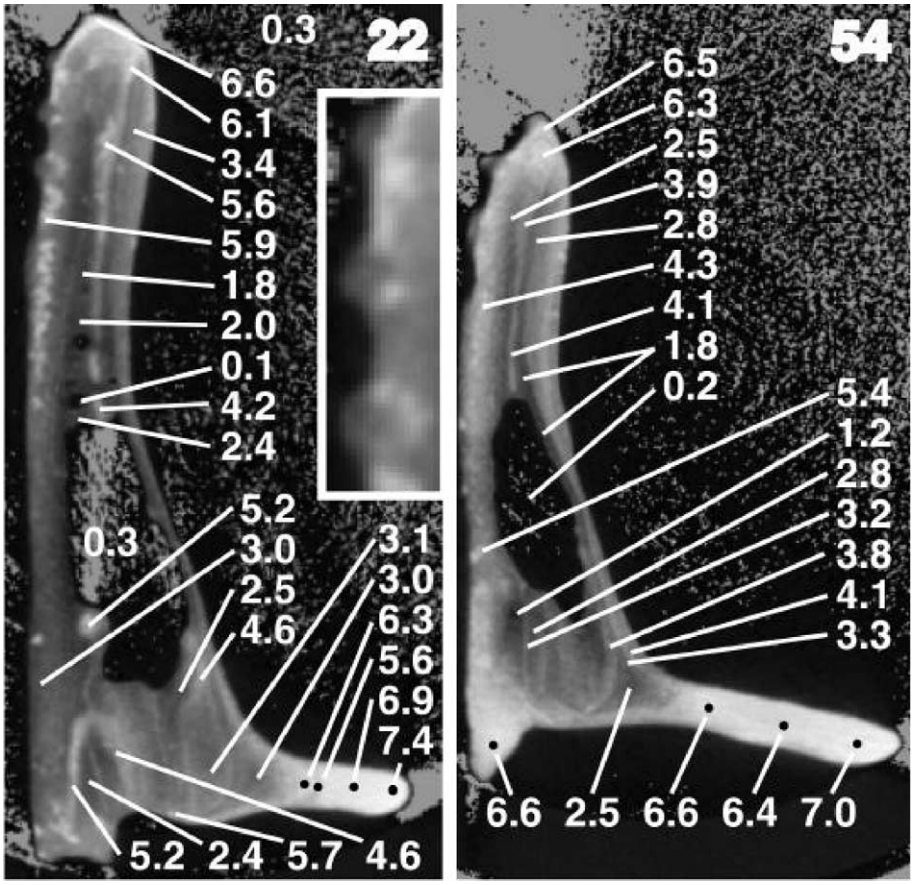

Fig. 7. Slice 22 (left) and slice 54 (right) of demipyramid 3 labeled with values of the linear attenuation coefficient (cm^{-1}). The slices are comprised of about 9 μm voxels (in-plane) and are about 10.5 and 13.8 mm, respectively, from the oral end of the demipyramid. The horizontal field of view is 3.6 mm in both images. The image inset on slice 22 enlarges the upper left surface of the slice.

pattern except in the tangential wall which is almost completely composed of voxels 6.4 cm^{-1} and higher.

Fig. 8 shows demipyramid 5 before (left) and after (right) infiltration with the polytungstate solution; except for a slight amount of tilt, the two images are at matching positions. The gray area (lower right of the infiltrated sample) is the polytungstate fluid, and its linear attenuation coefficient (3.6 cm^{-1}) is midway between the extremes in this slice prior to infiltration (7.4 cm^{-1} in the tangential wall and 0.3 cm^{-1} in the intrapyramidal cavity) and is almost exactly that of the low absorptivity stereom in the uninfiltrated sample. The low absorptivity volumes of the demipyramid increase from 3.4–3.5 to 4.9 cm^{-1} following infiltration in one location and from 2.5–2.8 to 4.8 cm^{-1} at another; within the intrapyramidal cavity the increase is from 0.3 to 3.5 cm^{-1}.

4. Discussion

The foramen magnus of the camarodont pyramid saves considerable weight (and decreases the amount of calcite the sea urchin must produce) compared to cidarid pyramids. Its introduction significantly shortens the pyramidal suture which, in the absence of any other compensating structural modification, weakens the lantern considerably. The epiphyses of camarodonts, which close the gap across the top of the foramen magnus, join in a suture and brace the structure (Figs. 2–4). The epiphyseal crest restrains the tooth at a point far removed from the dental slide (Jackson, 1912), increasing resistance to bending and to prying the teeth from the pyramid. The crest offers as wide an attachment area as the dental slide and supports the tooth at a position where the keel has just begun to form.

The angles between the radial and tangential walls of *Paracentrotus lividus* (Bonasoro and Candia Carnevali, 1994) and *L. variegatus* demipyramids are both about 100°; note that Fig. 3b of Candia Carnevali et al. (1991) is misleading and Fig. 3 of Bonasoro and Candia Carnevali (1994) shows the actual angle more accurately. It would be surprising if a gross difference were present in two camarodont lanterns, but there are minor differences in the outer envelope of the two demipyramids. Fig. 9 compares microCT slices of *L. variegatus* to schematics of cross sections of *P. lividus* for several longitudinal positions (after Märkel, 1976), and minor

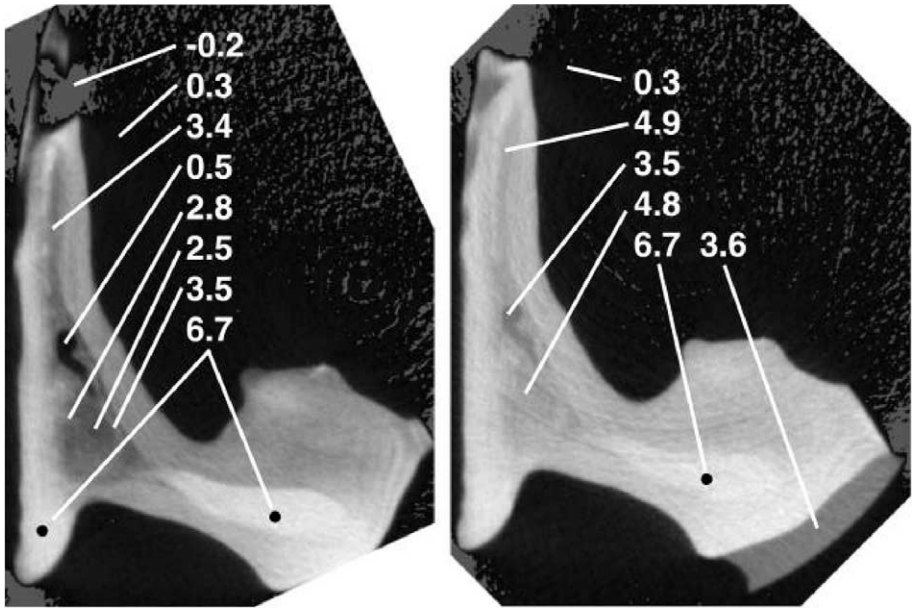

Fig. 8. Slice about 8.1 mm from the oral end of the demipyramid 5 before (left) and after (right) infiltration with polytungstate solution. The vertical field of view is 5.5 mm in both images, and the slice consists of 11 μm voxels (in-plane).

exterior differences are clear as is the much larger (and deeper) intrapyramidal cavity "ic" in *L. variegatus*. Here, the tracings are only intended to match the slices in a general way.

Before discussing the fine structure within the microCT slices, it is appropriate to explicitly address the issue of accuracy of the computed tomography approach to reconstructing cross sections of a sample. Some time ago, Kinney and Nichols (1992) went to the trouble of sectioning a ceramic matrix composite sample at the same position where a synchrotron microCT slice had been recorded; within the limitations of the detector and the spatial resolution of the reconstruction, the only differences were small artifacts from sample polishing and slight misorientation of plane of the microCT slice and the polished surface. Aside from a minor loss of contrast due to use of an X-ray tube instead of monochromatic synchrotron X-radiation, the laboratory microCT slices on which this study is based will be no less exact.

A pattern of long, linear features with alternating high and low absorption coefficients appears on either side of the epiphyseal suture (Figs. 3 and 4). Most of the lower absorption areas produce contrast similar to that of the stereom away from the suture area, but there are occasional pockets of very low absorption (both epiphyses in slice 338, the lower epiphysis in slice 370) with in-plane dimensions substantially larger than the instrument's resolution limit. The individual linear features "l" are quite long but only several voxels across, and they probably rarely occupy entire voxels. In *P. lividus*, Candia Carnevali et al. (1991, Plate 5g) show a cross section through the epiphyseal suture where long, linear filaments stretch across the suture face; they interpreted these features as strong ligaments preserved after mild semidigestion of soft tissue in the sample. If the "ligaments" in *P. lividus* correspond to the long linear features in Figs. 3 and 4 of this work, then they are, in fact, calcite-containing structures of a very interesting variant of stereom. It is possible that the suture structure actually differs for these two camarodont species, and further work at higher spatial resolution is required, say with synchrotron microCT and voxel dimensions approaching 1 μm, before the *L. variegatus* microstructure producing the unusual images is more clearly revealed.

In Fig. 7, linear attenuation coefficient values range widely within the demipyramid. Because the demipyramid lay on the tank bottom for some time and was stored in air for several months prior to the microCT study, it is reasonable to assume that the stromal space is empty and that the observed range of linear attenuation coefficients results, at least in part, from a range of volume fractions of stromal space and stereom mineral. This assumption was confirmed in the penetrant experiment described below. There is a second possible source of the range of absorptivities, namely variation in Mg content in the calcite mineral phase, and this will be examined before changes in volume fraction of stereom are considered.

In order to calculate the linear attenuation coefficients for calcite containing different amounts of Mg, the mass attenuation coefficients μ/ρ for the different elements in the compound (at the effective energy of the X-ray beam) are needed as well as the density of the compound. For pure calcite ($Ca_{1-x}Mg_xCO_3$ with $x = 0$), powder diffraction file card 86-2343 gives the density $\rho = 2.72\,g/cm^3$. Mass attenuation coefficients tabulated by NIST (2001) yield $\mu = 7.5\,cm^{-1}$ for pure calcite (i.e.,

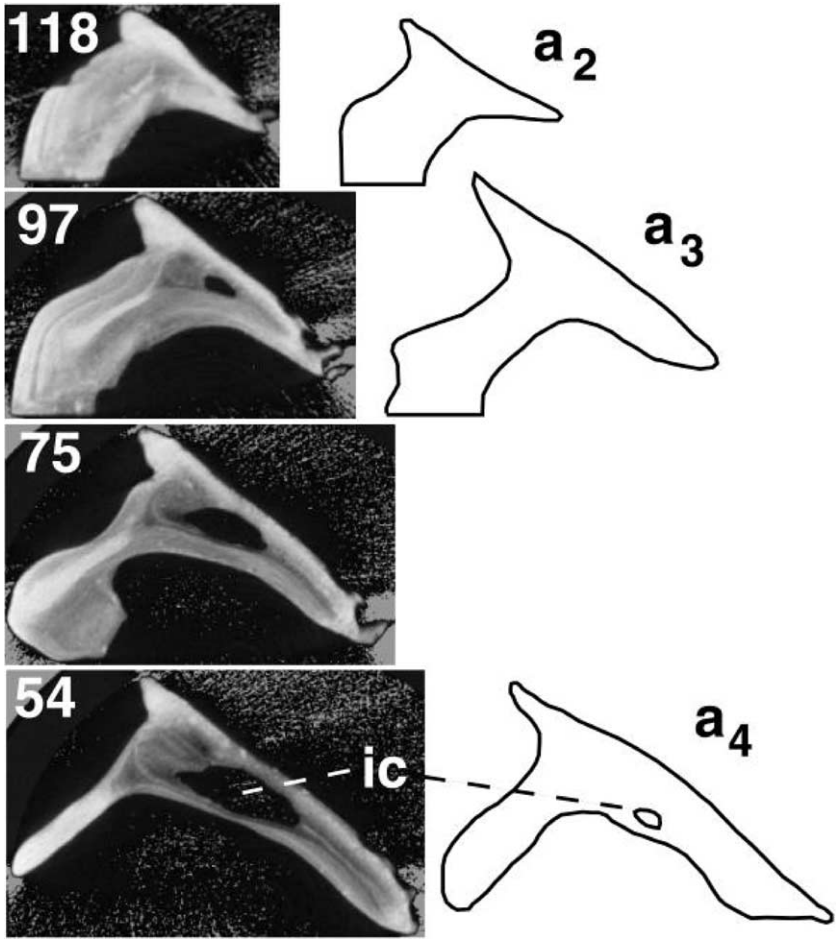

Fig. 9. Slices from *Lytechinus variegatus* (left column, demipyramid 3 with 9 μm voxels in-plane) compared with schematics of the cross section of *Paracentrotus lividus* (right column, based on portions of images $a_2 - a_4$ of Fig. 1 of Märkel, 1976). The separation between microCT slices was 100 μm, between a_4 and a_3 was 1.8 mm, and between a_3 and a_2 was 1.2 mm. The white numerals in the upper left-hand corner give the slice number, and the schematics are all at the same magnification, but adjusted for comparison with the microCT data. The horizontal field of view is 3.34 mm for the portion of slice 54 shown.

$x = 0$) for the effective X-ray photon energy (26 keV, 0.48 Å wavelength). For pyramids of *L. variegatus*, Weber (1969) gives $0.115 < w < 0.118$ for the wt fraction of Mg which corresponds to $\mu = 6.9$–$7.0\,\mathrm{cm}^{-1}$ if one assumes the same density as for calcite with $x = 0$; according to powder diffraction file cards 86-2336 ($x = 0.129$) and 86-2335 ($x = 0.064$), this introduces negligible error. The difference between these values is quite small and demonstrates that microCT cannot be a particularly good tool for precisely determining variation in Mg content in biogenerated calcite.

Assume for the purpose of discussion that volumes of fully dense calcite with $x = 0.5$, i.e., protodolomite, were responsible for the low absorptivity regions of the demipyramid. Proceeding as above, this material would have $\mu = 5.0\,\mathrm{cm}^{-1}$, a value considerably greater than that in a large part of the demipyramid. Except in fossils where diagenetic redistribution of Mg produces small pockets of dolomite ($x \sim 0.5$), e.g., reports of MacQueen and co-workers (1970, 1974) and Dickson (2001), compositions as high as $x \sim 0.45$ appear only in teeth (Schroeder et al., 1969), and variability in compositions in ossicles such as demipyramids, even measured with microscopic techniques, is on the order of percent Mg, not tens of percent (Weber, 1969). In terms of elements other than Mg with the greatest potential for altering linear attenuation coefficients in echinoderm ossicles (a combination of high atomic number and high concentration), DuBois and Chen (1989) and Smith (1990) indicate Sr, observed at concentrations up to 1 wt% (Weber, 1969), is the only realistic possibility. Assuming density unchanged from that of pure calcite and taking $Ca_{1-y}Sr_yCO_3$ with $y = 0.01$ (slightly less than 1 wt%) yields $\mu = 8.1\,\mathrm{cm}^{-1}$ at 26 keV (the atomic weight and linear attenuation coefficient of Sr are more than twice and nearly five times as great, respectively, as those of Ca), a change in the opposite direction from that required to explain the large number of voxels with $\mu = 5.0\,\mathrm{cm}^{-1}$. Therefore, neither variation in Mg nor in other elements can be responsible for the observed range

of absorptivities in the demipyramids, and almost all of the observed variation of linear attenuation coefficient must be due to changes in mineral volume fraction.

Before turning to conversion of values of linear attenuation coefficient to volume fraction of mineral, consider the spatial distribution of high and low density stereom within the demipyramid and possible reasons underlying its formation. The narrow portion of the tangential wall in Fig. 7, for example, consists of very dense material; it borders the foramen magnus and must carry the forces which would have been carried by the missing section of wall. The increased mineral density adoral from slice 54 (Figs. 8 and 9) reflects similar mechanical considerations. The role of the fine bands of high absorption structure between the intrapyramidal cavity and the corner where the radial and tangential walls meet is obscure and may reflect growth bands (Becher, 1924; Ebert, 1988a,b; Jensen, 1969; Märkel, 1976, 1979; Pearse and Pearse, 1975; Smith, 1980) or structural reinforcement bands (Becher, 1924) which are reported in sea urchin stereom. It is plausible that the narrow band of high absorptivity stereom running the length of the radial wall serves to strengthen the "hollow tube" of the radial wall against buckling; strictly speaking, the radial wall is not hollow, but for the much lower interior vs outer stereom density this is not too inaccurate.

The maximum linear attenuation coefficient in Fig. 6 is $7.4\,\mathrm{cm}^{-1}$, a value somewhat higher than that expected, and this is representative of other slices. The difference between calculated and observed linear attenuation coefficients for $Ca_{1-x}Mg_xCO_3$ is not surprising, given the approximate nature of any effective energy determined for a nonmonochromatic X-ray beam. Air produces $0.15 < \mu(\mathrm{cm}^{-1}) < 0.4$; this includes values in the intrapyramidal cavities. Linear attenuation coefficient differences smaller than about $0.4\,\mathrm{cm}^{-1}$, therefore, cannot be regarded as significant.

Providing that the microCT data were sufficiently sensitive, volume fractions of high contrast features can be obtained down to 0.1 voxel (Breunig et al., 1992, 1993). Accordingly, the fraction of a voxel occupied by stereom (calcite) f was determined from the relationship (Guvenilir et al., 1997)

$$f = \frac{\Delta V}{V} = 1 - \frac{\mu_s - \mu_{obs}}{\mu_s},$$

where μ_s is the value of the linear attenuation coefficient for a voxel occupied entirely by mineral (in this context "s" denotes stereom) and μ_{obs} is the value observed. The most straightforward approach, and probably the most accurate given the uncertainties cited above, is to take $\mu_s = 7.4\,\mathrm{cm}^{-1}$ as representative of voxels of stereom completely occupied by calcite with 0.11–0.12 wt fraction Mg.

In the pair of slices shown in Fig. 7, the linear attenuation coefficients correspond to volume fraction f of mineral $0.25 < f < 1.00$. Specifically, μ equaling 7.0, 6.4, 3.8, 2.5, $1.8\,\mathrm{cm}^{-1}$ correspond to mineral fractions of 95, 86, 51, 34, 24%, respectively. The corners and ends of the "L"-shaped demipyramid have $f > 0.8$, and often $f > 0.9$ in these regions. The volume fraction of stereom is not only a strong function of position within each longitudinal plane of a demipyramid (i.e., within each), but the mean volume fraction in each slice also rises significantly as one moves adorally from slices containing the intrapyramidal cavity to the apex of the pyramid. In the present instance (demipyramid 3) this increase occurs with increasing slice number. In slice 22 of demipyramid 3, the mean volume fraction of mineral is 0.39 if the intrapyramidal cavity is included and 0.46 if it is explicitly excluded. In slice 107 of demipyramid 3, which is slightly adoral in position from that shown in Fig. 8 and which does not intersect the interpyramidal cavity, the volume fraction of mineral is 0.70.

Comparisons of linear attenuation coefficients before and after infiltration of the stereom (e.g., demipyramid 5 in Fig. 8) provide a check of the volume fraction of porosity present. Direct comparison of linear attenuation coefficients of voxels before and after infiltration (3.4, 2.5–2.8, $0.5\,\mathrm{cm}^{-1}$ vs 4.9, 4.8, $3.5\,\mathrm{cm}^{-1}$, respectively) agrees to better than 10 vol%, that is, the linear attenuation coefficients are lower by an amount consistent with 2–10 vol% of residual empty space or soft tissue (not filled with polytungstate fluid) within the stereom. There is a real possibility of trapping a significant amount of air bubbles within the very microporous structure, and these results, therefore, demonstrate the values of local mineral volume fraction derived from the experimental linear attenuation coefficient are accurate.

Weber (1969) precisely measured the volume fraction of porosity in different echinoid ossicles of *Heterocentrotus mammillatus* (two individuals from different locations) and of *Diadema setosum*; density measurements were by weighing dry samples of ossicles and by measuring their displacement. Test porosity ranged from 28 to 30% while porosity of the primary spines of *Heterocentrotus* was 45–52% and of *Diademia* was 13% and reflected the very different architectures of these spines. Pyramids showed 16–17 and 11% porosity for *Heterocentrotus* and *Diademia*, respectively, and epiphyses showed 14–17 and 12% porosities, respectively. These measurements were macroscopic and do not reflect density variations on a microscopic scale.

H. mammillatus is a camarodont sea urchin and, all things being equal, porosities would be expected to be similar to those in *L. variegatus*. Instead, there is a substantial difference in mineral volume fraction: about 0.85 reported for the former and a range between 0.45 and 0.70 for the latter. The measurements are from very different techniques, and, from the details provided in the earlier work (Weber, 1969), it is difficult to decide whether the volume fractions truly differ or whether

systematic difference in what is measured by the two approaches produces the difference. Resolution of this question must await microCT study of *H. mammillatus* demipyramids.

Weber (1969) also found 5 wt% Mg in pyramids of *H. mammillatus*, somewhat less than one-half of that reported in *L. variegatus*. Differences of this scale suggest that the two species chose different composite design strategies for their pyramids, and this may be related to the possible difference in volume fraction of mineral described above. Higher Mg contents in calcite are linked to higher strength of sea urchin ossicles, and it is attractive to view the higher Mg content in *L. variegatus* (compared to *H. mammillatus*) as compensating for its lower mineral density.

Microscopic variation in mineral volume fraction may be tied to changes in stereom type or to thicker trabeculae combined with narrower pores. For the exterior surface of test plates, different relationships between trabecular thickness and pore diameter have been demonstrated for several sterom microarchitectures, and the range of trabecular thicknesses for a given pore diameter can be quite large. (Smith, 1980; Smith, 1990). In transverse and longitudinal cross sections of demipyramids of *P. lividus*, a camarodont sea urchin not unlike *L. variegatus*, Candia Carnevali and co-workers (1991) mapped the stereom types and found the following for sections corresponding to those in Fig. 7. Galleried stereom covered the outer radial wall, the corner between radial and tangential walls, and the half of the tangential wall closest to the corner. Fasicular stereom backed the galleried stereom and extended beyond it to the end of the tangential and radial walls. A large portion, but not all, of the inner walls was covered by microperforate stereom, and labryrinthic material filled the center of the tangential wall. The intrapyramidal cavity was lined by laminar stereom, and labyrinthic stereom surrounded the laminar zone around the intrapyramidal cavity and formed the portion of the inner walls closest to the intersection of radial and tangential walls.

The protuberances on the outer tangential wall of the demipyramid (inset image of Fig. 7) are the intrapyramidal muscle attachment ridges (seen in Fig. 2, left) and consist of low absorptivity material. High absorptivity voxels (described as "nodules" under Section 3) are adjacent to the ridges and occupy positions where the ridges merge into the wall. The distribution of mineral appears to be reversed for that observed in *P. lividus*. In the attachment area for the interpyramidal muscles of *P. lividus*, Candia Carnevali et al. (1991) found a specialized type of galleried stereom: longitudinally aligned and parallel trabeculae followed the arrangement of muscle fibers; i.e., the trabeculae axes were perpendicular to the ridge axes. The lower magnification micrographs of the ridges (Plates 3a, 3b, and 3d of Candia Carnevali et al., 1991) appear to contain a higher density of mineral; at higher magnification (Plate 3c), this may be the case, but the dominant impressions are that the trabecular array is much more regular in the ridges than in the area between them and that there is little difference in density of trabecular structure.

Fig. 10 shows SEM images of the interpyramidal muscle attachment surface of *L. variegatus*. The structure is similar to that observed previously in *P. lividus* (Candia Carnevali et al., 1991). The top image of Fig. 10 shows two ridges flanking a single valley, and the lower image is a higher magnification view of a valley in a second area. The demipyramid's stay on the aquarium bottom and handling apparently damaged the stereom on the ridge surfaces. In contrast, the stereom in the valleys remains more clearly delineated, and visual comparison of the damaged and undamaged surfaces is problematic if the goal is identifying differences in stereom volume fraction.

Stereom microarchitecture is too fine for the current generation of laboratory microCT scanners to resolve, at least within intact demipyramids of *L. variegatus*. In one sense this is an advantage: gradients in mineral volume fraction can be visualized readily as smoothly varying changes in absorptivity. Such changes could be measured with SEM, but detecting such long-range variations superimposed on a highly variable population of trabeculae and pores is intrinsically difficult when relying upon measurements of dimensions of individual trabeculae and pores. Further, 3-D interrogation would require examining many sections, and such serial sectioning of microporous materials is extremely difficult unless the porosity is first filled by epoxy or other filler. Accurate volume fractions of mineral could then be obtained at the cost of considerable labor, but the ability to distinguish different stereom types at a glance would be lost.

Synchrotron microCT provides spatial resolution approaching 1 μm for samples with cross sections ~2 mm wide; and this is sufficient for imaging individual trabeculae of the stereom within the interior of ossicles. Recently, fragments of a demipyramid of *L. variegatus* were imaged with synchrotron microCT and the stereom microarchitecture was resolved clearly (Stock et al., 2002c). Such 3-D data present new challenges, including development of sensible measures of *local* stereom volume fraction, of *local* measures of the distributions of trabecular orientation (and of the corresponding quantity for pores), and of *local* measures of the shape of trabecular elements of the stereom. Obtaining such quantities underlies much of the microarchitectural work done on the mechanical competence of bone and on bone's response to aging and to various therapeutic agents (e.g., Odgaard, 1997). Adaptation of such methodology appears very promising for differentiating different stereom types and for quantifying changes in stereom element dimensions employed to optimize ossicle functionality.

The gradients in mineral volume fraction within the demipyramid revealed in this study appear to have been

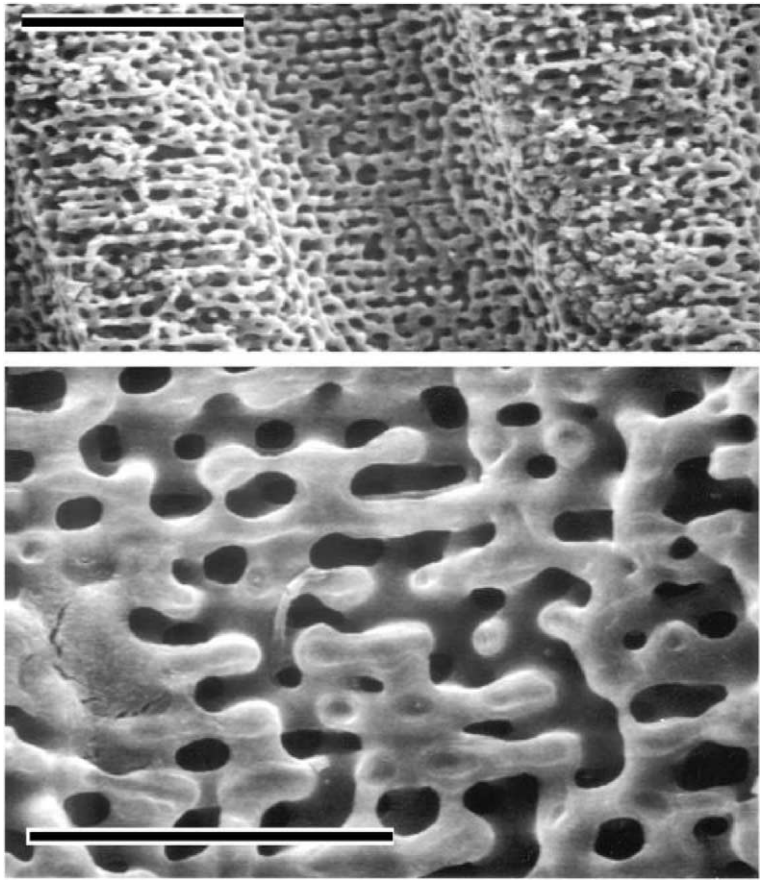

Fig. 10. SEM micrographs of interpyramidal muscle attachment surface of a demipyramid of *Lytechinus variegatus.* The secondary electron images were recorded with 25 kV electrons. (Top) Two ridges separated by a valley. The scale bar is 100 μm in length. (Bottom) Higher magnification view of the stereom in a second valley area. The scale bar is 20 μm long.

largely unremarked, with prior discussion of stereom variation largely being focused on the distribution of different microarchitectural types, e.g., measurements of Smith (1980) on average pore size vs minimum trabecular thickness for different positions in test plates. The variations reported in the present paper concern the structure as an entirety, and the demipyramid is seen to be a functionally graded structure. This grading is probably the result of both micromechanical optimization and of growth-related variations in trabecular dimensions. These gradients underlie the performance of the demipyramid as a mechanical structure, and the numerical data on mineral content as a function of 3-D position can serve as the input for powerful finite element models of the structure. These might be similar to microCT-based modeling of mechanical responses of mammalian trabecular bone to applied loads (e.g., Hildebrand et al., 1997; Ladd and Kinney, 1997). Muscle insertion sites in the lantern and spine and connected ossicles (Candia Carnevali et al., 1993; Märkel, 1976; Märkel and Röser, 1983; Smith et al., 1990) would be one profitable (and tractable, in terms of computational complexity) area for numerical modeling.

Numerical data on the 3-D distribution of mineral also allow important numerical inferences on the operation of the cellular processes generating the mineral, much like those made from microCT data of chemical vapor infiltration of ceramic composites based on woven preforms (Kinney et al., 1993; Lee et al., 1998). MicroCT offers the prospect, for the first time, of in vivo observation of the same internal ossicle at different stages of growth. In other words, it should be possible to study temporal as well as spatial gradients of structure (assuming that the radiation dose to the sea urchin does not affect subsequent growth). The authors anticipate that use of such a temporal as well as spatial probe of evolving structure will greatly improve understanding of the development of sea urchin ossicles and biomineralization in general.

Acknowledgments

This work was partially supported by US NIH, National Institute of Dental and Craniofacial Research Grant DE-01374 (A.V.). Some of the data were collected at the Georgia Tech Microtomography Facility which is

supported by NSF BES Grant 9977551 (S.R.S.) and some at the Northwestern University MicroCT facility.

References

Becher, E., 1924. Über den feineren Bau der Skelettsubstanz bei Echinoideen, insbesondere über statische Strukturen in derselben. Zool. Jahrbuch (Abteilung Allgemeine Zool. Physiol.) 41, 179–244.

Bonasoro, F., Candia Carnevali, D.M., 1994. Atypical chordoid structures in Aristotle's lantern of regular echinoids. Acta Zool. (Stockholm) 75, 89–100.

Breunig, T.M., Elliott, J.C., Stock, S.R., Anderson, P., Davis, G.R., Guvenilir, A., 1992. Quantitative characterization of damage in a composite material using X-ray tomographic microscopy. In: X-ray Microscopy III. Springer-Verlag, New York, pp. 465–468.

Breunig, T.M., Stock, S.R., Guvenilir, A., Elliott, J.C., Anderson, P., Davis, G.R., 1993. Damage in aligned fibre SiC/Al quantified using a laboratory X-ray tomographic microscope. Composites 24, 209–213.

Candia Carnevali, D.M., Bonasoro, F., Melone, G., 1991. Microstructure and mechanical design in the lantern ossicles of the regular sea-urchin *Paracentrotus lividus*: A scanning electron microscope study. Bull Zool. 58, 1–42.

Candia Carnevali, D.M., Wilkie, I.C., Lucca, E., Andretti, F., Melone, G., 1993. The Aristotle's lantern of the sea-urchin *Stylocidaris affinis* (Echinoida, Cidaridae): Functional morphology of the musculo-skeletal system. Zoomorphology 113, 173–189.

Dickson, J.A.D., 2001. Transformations of echinoid Mg calcite skeletons by heating. Geochim. Cosmochim. Acta 65, 443–454.

DuBois, P., Chen, C.-P., 1989. Calcification in echinoderms. Echinoderm Stud. 3, 109–178.

Ebert, T.A., 1988a. Calibration of natural growth lines in ossicles of two sea urchins. *Strongylocentrotus purpuratus* and *Echinometra mathei*, using tetracycline. In: Burke, et al. (Eds.), Echinoderm Biology. Balkema, Rotterdam, pp. 435–443.

Ebert, T.A., 1988b. Growth, regeneration and damage repair of spines of the slate-pencil sea urchin *Heterocentrotus mammillatus* (L.) (Echinodermata: Echinoidea). Pac. Sci. 42, 160–172.

Guvenilir, A., Breunig, T.M., Kinney, J.H., Stock, S.R., 1997. Direct observation of crack opening as a function of applied load in the interior of a notched tensile sample of Al-Li 2090. Acta Mater. 45, 1977–1987.

Hildebrand, T., Laib, A., Ulrich, D., Kohlbrenner, A., Rügsegger, P., 1997. Bone structure as revealed by microtomography. In: Bonse, U. (Ed.), Developments in X-ray Computed Tomography, SPIE, vol. 3149, pp. 34–43.

Jackson, R.T., 1912. Phylogeny of the Echini with a revision of Palaeozoic Species. Memoirs of the Boston Society of Natural History, vol. 7, pp. 1-491, plates 1-72.

Jensen, M., 1969. Age determination of echinoids. Sarsia 37, 41–44.

Kinney, J.H., Nichols, M.C., 1992. X-ray tomographic microscopy (XTM) using synchrotron radiation. Annu. Rev. Mater. Sci. 22, 121–152.

Kinney, J.H., Breunig, T.M., Starr, T.L., Haupt, D., Nichols, M.C., Stock, S.R., Butts, M.D., Saroyan, R.A., 1993. X-ray tomographic study of chemical vapor infiltration processing of ceramic composites. Science 260, 789–792.

Ladd, A.J.C, Kinney, J.H., 1997. Elastic constants of cellular structures. Physica A240, 349–360.

Lee, S.-B., Stock, S.R., Butts, M.D., Starr, T.L., Breunig, T.M., Kinney, J.H., 1998. Pore geometry in woven fiber structures: 0E/90E plain-weave cloth lay-up preform. J. Mater. Res. 13, 1209–1217.

MacQueen, R.W., Ghent, E.D., 1970. Electron microprobe study of magnesium distribution in some Mississippian echinoderm limestones from western Canada. Can. J. Earth Sci. 7, 1308–1316.

MacQueen, R.W., Ghent, E.D., Davies, G.R., 1974. Magnesium distribution in living and fossil specimens of the echinoid *Peronella lesueuri* Agassiz, Shark Bay, Western Australia. J. Sedimentary Petrol. 44, 60–69.

Märkel, K., 1969. Morphologie der Seeigelzähne: II. Die gekielten Zähne der Echinacea (Echinodermata, Echinoidea). Z. Morphol. Tiere 66, 1–50.

Märkel, K., 1970a. Morphologie der Seeigelzähne: III. Die Zähne der Diadematoida und Echinothuroida (Echinodermata Echinoidea). Z. Morphol. Tiere 66, 189–211.

Märkel, K., 1970b. Morphologie der Seeigelzähne: IV. Die Zähne von *Laganum und Clypeaster* (Echinodermata, Echinoidea). Z. Morphol. Tiere 68, 370–389.

Märkel, K., 1976. Das Wachstum der, "Laterne des Aristoteles" und seine Anpassung an die Funktion der Laterne (Echinodermata, Echinoidea). Zoomorphologie 86, 25–40.

Märkel, K., 1979. Structure and growth of the cidaroid socket-joint Lantern of Aristotle compared to the hinge-joint lanterns of non-cidaroid regular echinoids (Echinodermata, Echinoidea). Zoomorphologie 94, 1–32.

Märkel, K., Titschack, H., 1969. Morphologie der Seeigelzähne: I. Der Zahn von *Stylocidaris affinis* (Phil.) (Echinodermata, Echinoidea). Z. Morphol. Tiere 64, 179–200.

Märkel, K., Röser, U., 1983. The spine tissues in the echinoid *Eucidaris tribuloides*. Zoomorphology 103, 25–41.

Märkel, K., Gorny, P., Abraham, K., 1976. Microarchitecture of sea urchin teeth. Fortschr. Zool. 24, 103–114.

NIST, Tables of X-ray Mass Attenuation Coefficients and Mass Energy Absorption Coefficients from 1 keV to 20 MeV for Elelments Z = 1 to 92 and 48 Additional Substances of Dosimetric Interest, NISTIR 5632, July 2001.

Odgaard, A., 1997. Three-dimensional methods for quantification of cancellous bone architecture. Bone 20, 315–328.

Pearse, J.S., Pearse, V.B., 1975. Growth zones in the echinoid skeleton. Am. Zool. 15, 731–753.

Schroeder, J.H., Dwornik, E.J., Papike, J.J., 1969. Primary protodolomite in echinoid skeletons. Bull. Geol. Soc. Am. 80, 1613–1616.

Smith, A.B., 1980. Stereom microstructure of the echinoid test, Special papers in Palaeontology No. 25. The Palaeontology Association, London.

Smith, A.B., 1984. Echinoid Palaeobiology. Allen and Unwin, London.

Smith, A.B., 1990. Biomineralization in echinoderms. In: Carter, J.G. (Ed.), Skeletal Biomineralization: Patterns, Processes and Evolutionary Trends. Van Nostrand Reinhold, New York, Chapter 17 of vol. I, pp. 413–443 and vol. II, Pt. 8, pp. 69–71 and Pl. 170–175.

Smith, D.S., del Castillo, J., Morales, M., Luke, B., 1990. The attachment of collagenous ligament to stereom in primary spines of the sea urchin *Eucidaris tribuloides*. Tissue Cell 22, 157–176.

Stock, S.R., 1999. Microtomography of materials. Int. Mater. Rev. 44, 141–164.

Stock, S.R., Dahl, T., Barss, J., Veis, A., Fezzaa, K., Lee, W.K., 2002a. Mineral phase microstructure in teeth of the short spined sea urchin (*Lytechinus variegatus*) studied with X-ray phase contrast imaging and with absorption microtomography. Adv. X-ray Anal. 45, 133–138.

Stock, S.R., Dahl, T., Barss, J., Veis, A., Almer, J.D., 2002b. X-ray absorption microtomography (microCT) and small beam diffraction mapping of sea urchin teeth. J. Struct. Biol. 139, 1–12.

Stock, S.R., DeCarlo, F., Ignatiev, K., Dahl, T., Veis, A., 2002c, unpublished data.

Wang, R.Z., Addadi, L., Weiner, S., 1997. Design strategies of sea urchin teeth: Structure, composition and micromechanical relations to function. Philos. Trans. R. Soc. London B 352, 469–480.

Weber, J.N., 1969. The incorporation of magnesium into the skeletal calcites of echinoderms. Am. J. Sci. 267, 537–566.